journal of the mechanical behavior of biomedical materials 144 (2023) 105939

Contents lists available at ScienceDirect

Journal of the Mechanical Behavior of Biomedical Materials

journal homepage: www.elsevier.com/locate/jmbbm

Strength and ductility loss of Magnesium-Gadolinium due to corrosion in physiological environment: Experiments and modeling

Dirk Steglich [a,*], Jacques Besson [b], Inken Reinke [a], Heike Helmholz [c], Monika Luczak [c], Vasil M. Garamus [c], Björn Wiese [c], Daniel Höche [d], Christian J. Cyron [a,e], Regine Willumeit-Römer [c]

[a] Institute of Material Systems Modeling, Helmholtz-Zentrum Hereon, Max–Planck-Str. 1, 21502 Geesthacht, Germany
[b] Centre des Matériaux, PSL Research University, Mines ParisTech, UMR CNRS 7633, BP 87, 91003 Evry Cedex, France
[c] Institute of Metallic Biomaterials, Helmholtz-Zentrum Hereon, Max–Planck-Str. 1, 21502 Geesthacht, Germany
[d] Institute of Surface Science, Helmholtz-Zentrum Hereon, Max–Planck-Str. 1, 21502 Geesthacht, Germany
[e] Institute for Continuum and Material Mechanics, Hamburg University of Technology, Eissendorfer Str. 42, 21073 Hamburg, Germany

ARTICLE INFO

Keywords:
Biodegradable magnesium
Finite elements
Damage modeling
Corrosion localisation
Mass loss
Mg-10Gd

ABSTRACT

We propose a computational framework to study the effect of corrosion on the mechanical strength of magnesium (Mg) samples. Our work is motivated by the need to predict the residual strength of biomedical Mg implants after a given period of degradation in a physiological environment. To model corrosion, a mass-diffusion type model is used that accounts for localised corrosion using Weibull statistics. The overall mass loss is prescribed (e.g., based on experimental data). The mechanical behaviour of the Mg samples is modeled by a state-of-the-art Cazacu–Plunkett–Barlat plasticity model with a coupled damage model. This allowed us to study how Mg degradation in immersed samples reduces the mechanical strength over time. We performed a large number of in vitro corrosion experiments and mechanical tests to validate our computational framework. Our framework could predict both the experimentally observed loss of mechanical strength and the ductility due to corrosion for both tension and compression tests.

1. Introduction

Magnesium (Mg) and its alloys are becoming increasingly popular as alternatives to permanent implant materials due to their biodegradability, biocompatibility and ability to promote bone growth. Not only is the proven biocompatibility beneficial for tissue regeneration and consequently medical applications but also the documented osteoinductive and anti-inflammatory effects (Lin et al., 2022). Mg alloys have better mechanical properties and a better degradation behaviour than biodegradable polymers. Since the typically used alloying element Aluminium can be potentially neurotoxic, researchers are exploring the use of other alloying elements for implant materials. The use of aluminium-free magnesium alloys in biomedical implants depends on specific material properties, such as good biocompatibility, robust degradation behaviour, and suitable mechanical properties. Mg-Gd alloys have shown promising potential in terms of mechanical properties (Hort et al., 2010; Harmuth et al., 2019) and in vitro and in vivo biocompatibility testing (Feyerabend et al., 2010; Myrissa et al., 2016; Helmholz et al., 2021b; Krüger et al., 2021, 2022). Tailoring suitable degradation kinetics for specific applications remains the focus of current research. In the case of binary Mg-Gd alloys, a minimum corrosion rate was observed for Mg-10Gd (Hort et al., 2010) in aerated 1% NaCl solution. At higher concentrations of Gd, the corrosion rate increased (Zhang, 2020).

Computational modeling can be used to make predictions based on in vitro experiments, thus speeding up the development process of new implants if reliable models are developed. Various computational models of Mg degradation have been published to date, including physical, phenomenological, analytical, and machine learning-based models. Dahms et al. (2018) presented a simplified model based on the mass conservation law, but did not include chemical and electrochemical processes due to the analytical nature of the approach. Other studies used continuum damage mechanics (CDM) models to describe the effect of Mg degradation on a phenomenological level. Gastaldi et al. (2011) and Grogan et al. (2011) used CDM models to simulate the diffusion-controlled degradation of Mg-based absorbable stents. The CDM approach allows for the study of the micro-scale geometric discontinuities induced by degradation on the mechanical integrity of the overall specimen without explicitly modeling the moving boundary. For addressing the latter, it is required to include the corrosive medium in the analysis, see e.g. Grogan et al. (2014). In any

* Corresponding author.
E-mail address: dirk.steglich@hereon.de (D. Steglich).

https://doi.org/10.1016/j.jmbbm.2023.105939
Received 8 March 2023; Received in revised form 19 May 2023; Accepted 24 May 2023
Available online 1 June 2023

case, these approaches do not consider the electrochemical processes that occur during degradation, which may vary locally. As a result, CDM model needs to be calibrated for each combination of corrosive environment and material composition. A method for experimentally generating the required data was described by Boland et al. (2018) for the magnesium alloy WE43. The authors successfully predicted the strength reduction of tensile samples as a function of the mass loss caused by in vitro degradation. In the same spirit, the present work aims at extending the predictive capabilities of numerical tools towards the ductility quantified by the failure strain as a function of the corrosion time. Corrosion is regarded as initiation for strain localisation and damage initiation. In the following, a mass diffusion type analysis is utilised to model the degradation of a Mg-10Gd alloy. Similar to the procedure described in Hermann et al. (2022), a concentration field representing Faraday's dissolution-related phase change of magnesium is simulated by a mass loss analysis and subsequently mapped to a variable affecting the local strength in the domain. Based on such a configuration, a finite element simulation of compression tests and tensile tests is performed to analyse the global mechanical strength of the sample that remains at the given point in time due to the corrosion up to that point. In contrast to the mentioned work, here, the local strength loss and the damage variable are considered in general as independent. While the first one is directly taken from the mass loss analysis, the latter evolves during loading in the mechanical simulation. This allows for the realistic incorporation of surface defects resulting from corrosion into a simulation model, facilitating the analysis of their effects on the mechanical behaviour of standard samples.

2. Material

The Mg alloy with 10 wt% Gd (Mg-10Gd) was produced by direct chill casting followed by solid solution heat treatment and in-direct extrusion as described by Harmuth et al. (2019). In contrast to the previous work, a round bar of 6 mm was extruded. The parameters were chosen so that the properties are comparable to the material extruded at 400 °C with an exit speed of 3.3 m/min. The exit speed was identical to that of 10 mm rods and adjusted due to the different extrusion ratio. Therefore, this material was extruded at 0.8 mm/s with an extrusion ratio of 1:69 at 400 °C. Run-in and run-out of the extrudate were cut and not used in the following.

3. Experiments

To quantify the corrosion and its effect on the mechanical behaviour, two different sample geometries were considered: prismatic bars (4 mm × 4 mm × 8 mm), and prismatic sticks (2 mm × 2 mm × 50 mm), similar to those used in Boland et al. (2018). The first one served two purposes: it was used during immersion tests to determine the mass loss as a function of time and to do the subsequent compression testing. The latter served as a tool to characterise the tensile properties of the corroded material. Some samples were further examined before mechanical testing by computed tomography (CT). The samples are referred in the following as immersion bars (IB) and tensile sticks (TS), respectively. All samples were machined from the centre of the extruded rod with identical machining parameters to achieve reproducible and comparable surface quality. This state is referred to as "as-received" in the following. It is the typical status prior to mechanical testing, but not suited for corrosion experiments. The latter required a more specific surface preparation, see the following section.

A subset of IB samples were quasi-statically compressed up to a strain of 10% to investigate the effect of plastic deformation on the corrosion rate. These samples are referred to as "predeformed" in the following. Table 1 summarises the number of samples and the different stages of immersion considered.

3.1. Corrosion

The immersion tests were performed according to NACE/ASTM G31-12a (NACE, 2016) standard as described by Nidadavolu et al. (2016). Prior to immersion, the materials were treated according to Gawlik et al. (2018, 2019) to obtain a homogeneous surface. At first, all types of material were cleaned with organic solvents for 40 min in an ultrasound bath in n-hexane. This procedure was followed by etching with acetic acid (150 s in 125 g glacial acid per 0.5 l ultrapure water type I). The material was neutralised and cleaned by short dipping in 1 mol/L NaOH, ultrapure water type I and acetone. Finally, the material was cleaned again for 40 min in n-hexane before drying and weighting. This state is referred to as "as prepared", see Table 1. The weights of the immersion bricks were recorded at specific points in time to calculate the average degradation rates based on mass loss during immersion. These values can be used in the simulations assuming a negligible initiation phase contribution and a moderate localisation of corrosion and degradation with statistically distributed pitting events. In addition to that preparation, the ends of the tensile sticks were protected with 5 mm heat-shrink tubing before sterilisation and immersion.

The immersion test was performed under sterile and physiological conditions at 37 °C, 5% CO_2, 19.7% O_2, 95% relative humidity. The immersion medium consisted of DMEM + Glutamax Dulbecco's Modified Eagle's Medium, 4.5 g/L D-Glucose (Life Technologies), 10% Fetal Bovine Serum (FBS, Sigma Aldrich Chemie GmbH) and 1% Penicillin–Streptomycin (Thermo Fisher Scientific Inc.). To optimise the immersion vessel regarding the specimens' geometry, the immersion bricks were placed in 12-well microtiter plates in 3 mL; the tensile sticks were placed in T25 cell culture flasks in 8 mL. As the immersion test was pursued in a semi-static manner, the medium was changed twice a week for one to five weeks. The pH value and osmolality were monitored during media exchange. Additionally, the released Mg ion concentration was determined in the immersion medium supernatant by atomic absorption spectroscopy as described in Globig et al. (2020) using a flame AAS (Agilent 240 AA, Agilent Technologies) at a wavelength of 285.2 nm. A calibration curve ranging from 0.05 to 1.00 mg/L Mg was applied for quantification.

After the immersion test, the degradation products of the immersion bricks were removed with chromic acid (immersion for 10 min 180 g/L Chromium(VI) oxide in ultrapure water) to calculate their mass loss. Before and after this procedure, the weights of the immersion bricks were measured with an electronic balance (SBA 32, accuracy 0.1 mg, SCALTEC Instruments GmbH). In addition to the mass loss method, a uniform-type corrosion rate was calculated by dividing the mass loss Δm [g] through the product of the surface area A, the density of the sample and the time of immersion t. In case of the immersion bricks, an initial surface area of $A = 160\,\mathrm{mm}^2$ and a density of $\rho = 1.876\,10^{-3}\,\mathrm{g/mm}^3$ were taken.

3.2. Computed tomography

The X-ray computed tomography (CT) scans were performed on selected TS samples with the CT scanner YXLON Cougar (YXLON International GmbH). The scanner was equipped with an area detector of 1004 × 1004 pixels with a pixel size of 0.127 mm. During the scans, the samples rotated around the longitudinal axis. A compromise between relevant information and spatial resolution was made for the scanned volume. The scanned volume of the tensile sticks contained the central part with the length of 25 mm. Five of the immersion bricks (4 mm × 4 mm × 8 mm) were scanned as well to verify the segmentation (grey level). The immersion bricks were completely displayed by the CT scan. The following conditions were applied during all CT scans: voltage 60 kV, current 55 μA with 1200 projections (3 repetitions). The obtained voxel sizes were 0.0263 mm (tensile sticks) and 0.0149 mm (immersion bricks), respectively. Next, the CT scans were converted into a suitable format for further analysis.

Table 1
Test matrix (w: week).

Sample type	State	Comment	Corrosion time [w]	Number of samples
Immersion Bricks (IB)	as-received	carefully machined	–	6
	as prepared	etched for immersion	1, 2, 3, 4, 5	5 per corrosion time
	predeformed	compression prior immersion	1, 2, 3, 4, 5	5 per corrosion time ⇒ in total 56 IBs
Tensile Sticks (TS)	as-received	carefully machined	–	5
	as prepared	etched for immersion	1, 2, 3, 4, 5	5 per corrosion time ⇒ in total 30 TSs

Fig. 1. Applied segmentation masks: yellow — metallic part of the sample, green — corrosion product, turquoise — surrounding volume.

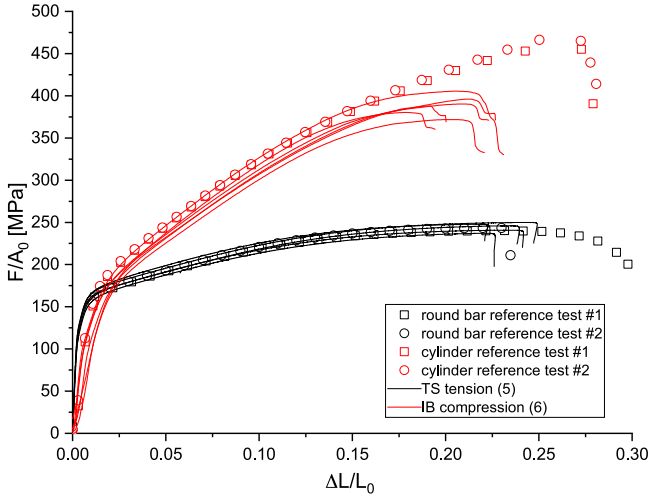

Fig. 2. Results of the tensile- and compression tests: standard samples (symbols) and TS/IB geometries (lines).

The CT scans were reconstructed with the YXLON Recoonspooler and converted into a DICOM format (Digital Imaging and Communications in Medicine) by VGSTUDIO MAX (Volume Graphics GmbH, Heidelberg, Germany). The software Simpleware (Synopsys, Inc.) was used to further edit and segment the reconstructed CT scans. Before segmentation, all scans were aligned and cropped to reduce the background. To segment the scans, multi-level Otsu segmentation was used that selects an optimal threshold with discriminant analysis applied on the histogram (Otsu, 1979). Three masks were chosen for segmenting the tensile stick scans, see Fig. 1. These masks represented the corroded sample (Mg-10Gd) (yellow), the corrosion product (green) and the surrounding area (turquoise). For the immersion bricks, only two masks were chosen because the corrosion product was removed from them. Subsequently, an FE discretisation was created in Simpleware with the mask of the corroded sample (Mg-10Gd). The FE model was exported to Abaqus via a standard input file (*.inp).

3.3. Mechanical testing

The tensile tests were conducted on a Zwick Roell Z0101 machine at a speed of 2 mm/min, with a maximum force of 2500 N and a preload of 0.3 N. While the force signal was acquired by the load cell, the displacement signal was recorded with the help of Electronic Speckle Pattern Interferometry, with a gauge length of approx. 6.5 mm. Additionally, the cross-head displacement was recorded. In the case of IB compression tests, a Schenck servo-hydraulic 1000 kN machine was used. Load was applied via mirror-polished parallel plates in axial direction, with a cross-head speed of 0.4 mm/min. Two extensometers were used to measure the relative displacement of the plates. The average of their readings was used to calculate the displacement along the compression direction. Stresses and strains reported in the following are understood as normalised forces (*i.e.*, force divided by the initial cross-section) and strains as length change divided by the initial length. Hence, they constitute global quantities, characterising samples as a whole.

To verify that the tests performed with our special sample geometries were mechanically meaningful and delivered results comparable to those of tests with standard sample geometries, a comparison on the basis of the as-received material was performed. Standard samples (smooth round bars and compression cylinders) were machined from the extruded material. Fig. 2 shows the results of tensile and compression tests performed on standard samples vs. the special samples used here. Apparently, the mechanical behaviour of both was nearly identical over a large strain interval. Since strain localisation is favoured in the case of TS and IB samples, these samples only failed at lower strains compared to the standard samples.

4. Modeling

Four subsequent steps were conducted to identify the data required to numerically predict the time-dependent strength loss. The strength loss is caused by uniform and localised degradation:

- Determination of the elastic–plastic behaviour of the as-received material by FE-simulations of tensile- and compression tests (no corrosion),
- Mapping of the shape of corroded tensile samples determined by CT scans to respective FE-models, segmentation and discretisation of the remaining metal, simulation of the individual tensile tests,
- Prediction of the remaining metallic magnesium in the samples as a function of time by phenomenological mass loss analyses, mapping of the magnesium concentration fields at distinct instances in time during the degradation period to fields generating a mechanical effect,
- Simulation of the mechanical behaviour of tensile and compression samples on the basis of a damage model to predict the strength loss effect induced by corrosion.

For the two latter points, statistical effects were investigated by considering Weibull-distributions of the surface flux leading to localisation

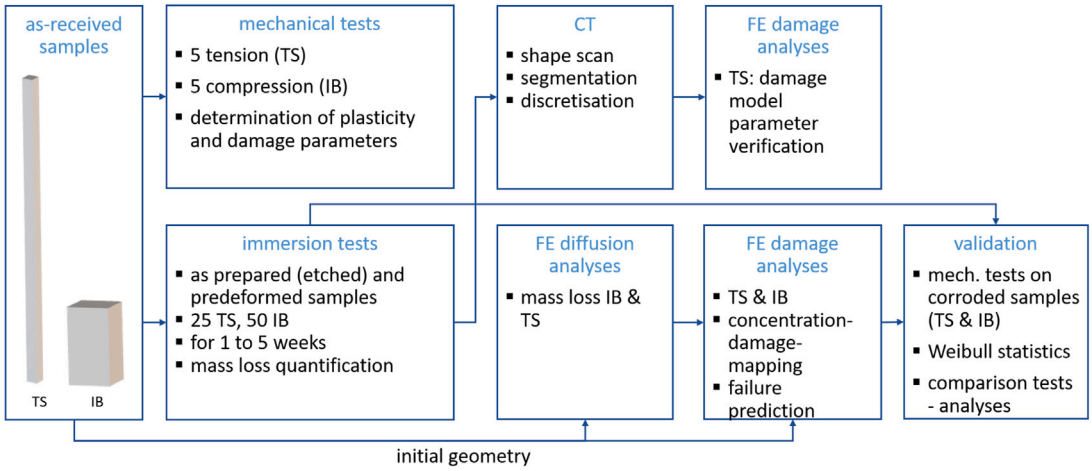

Fig. 3. Sequence of activities for the modeling.

of mass loss, one cause for pitting corrosion (Jafarzadeh et al., 2019). The description of pitting corrosion of aluminium via Weibull statistics was discussed by Gazenbiller et al. (2021). The flow of data described above is depicted in Fig. 3.

4.1. Mechanical behaviour: Plasticity and damage

Tensile and compression tests of the as-received material were used to calibrate a plasticity model. Due to the texture-induced asymmetry in tension and compression, the Cazacu–Plunkett–Barlat (CPB)-model (Cazacu et al., 2006) was selected for describing the irreversible time-independent deformation. Since the extrusion direction (ED) was the main loading direction and no information on other deformation modes apart from tension/compression along the ED was available, the original isotropic version of the CPB-model was used. The CPB-model was combined with a damage model on the basis of a weak coupling approach to predict damage nucleation and failure numerically. To this end, the effective stress of the CPB-model was used to define a yield surface by a plastic potential

$$\Phi\left(\boldsymbol{\sigma}, d, \sigma_F\right) = 0. \tag{1}$$

Here $\boldsymbol{\sigma}$ is the Cauchy stress tensor, d the internal damage variable, and σ_F the flow stress of the undamaged (matrix) material, which changes in general with the accumulated plastic strain.

The weak coupling between plasticity and damage was achieved by defining the yield surface as

$$\Phi = \frac{\overline{\sigma}}{\sigma_F} - (1 - d) = 0 \tag{2}$$

and using the following definition of an "equivalent stress" $\overline{\sigma}$

$$\overline{\sigma} = \left(\left(|s^1| - k s^1\right)^\kappa + \left(|s^2| - k s^2\right)^\kappa + \left(|s^3| - k s^3\right)^\kappa \right)^{1/\kappa} \quad , \tag{3}$$

where s^1, s^2 and s^3 are the eigenvalues of the deviator of $\boldsymbol{\sigma}$, κ controls the shape of the yield surface, and k the strength differential effect ($-1 < k < 1$). The flow stress of the material was expressed by a function of the accumulated plastic strain p as:

$$\sigma_F(p) = R_0 + Q_1(1 - \exp\left[-b_1 p\right]) + Q_2(1 - \exp\left[-b_2 p\right]) \quad . \tag{4}$$

Damage evolution was assumed to be controlled solely by the plastic strain via a damage nucleation function $\dot{d}_{nuc}$ (Chu and Needleman, 1980), hence:

$$\dot{d} = \dot{d}_{nuc} = \frac{d_n}{s_n\sqrt{2\pi}} \exp\left[-\frac{1}{2}\left(\frac{p - \varepsilon_n}{s_n}\right)^2\right] \dot{p} \quad . \tag{5}$$

The modulus of elasticity E_0 for isotropic elasticity was determined by using a resonant frequency and damping analyser on solution annealed Mg-Gd alloys with different Gd contents and assumed to be to 44.25 GPa (Xu et al., 2018). Poisson's ratio ν was set to 0.3. The model parameters κ, k, R_0, Q_1, b_1, Q_2, b_2, ε_n, d_n, s_n were calibrated by fitting stress–strain data of the finite-element simulations to the experimental results of the as-received (*i.e.* uncorroded) samples.

4.2. Diffusion-type model for mass loss prediction

The corrosion process was simulated by means of a three-dimensional diffusion-based model. The diffusion process representing the faradaic dissolution of magnesium samples was simulated through the finite element method according to Fick's second law

$$\frac{\partial c}{\partial t} = D\,\Delta c \quad , \tag{6}$$

where c is the magnesium concentration, t the time, D the coefficient of isotropic diffusion and Δ the Laplace operator. Following the procedure outlined in Grogan et al. (2011) and Marvi-Mashhadi et al. (2021), nodal concentration fluxes J_i on the surface of the samples were randomised with the use of the probability density function q of the Weibull distribution and a scaling factor β to simulate localised and pitting corrosion. The concentration fluxes J_i act as Neumann boundary conditions of the diffusion problem. The negative sign represents the flow direction out of the solid:

$$J_i = -\beta\, q(x_i) \quad \text{with} \tag{7}$$

$$q(x_i) = a\left(x_i\right)^{a-1} \exp\left(-(x_i)^a\right), \tag{8}$$

with a being the shape parameter of the distribution.

To achieve a prescribed mass loss at a given time in the simulation, the scaling factor β was introduced in Eq. (7) and calculated via

$$\beta \sum_i J_i = J_{tar}\,. \tag{9}$$

J_{tar} is the target overall flux preset and defines the integral/summation of all nodal fluxes. The concentration fluxes are connected to the change in concentration by Fick's law, Eq. (6). On this basis, the concentration at every integration point of each element can be calculated as a function of time. The global mass loss can be determined from the product of the concentration c_i and volume V_i in the integration points of the elements. The outcome is the amount of substance n_i in this particular integration point. Summing up the amount of substance of each integration point results in the current amount of substance at time t.

The corrosion process goes along with the formation of $Mg(OH)_2$ holding no mechanical relevance according to Marvi-Mashhadi et al. (2021). Therefore, concentrations less than $\alpha\, c_{MgGd}$ of the initial molar density c_{MgGd} were not considered in the summation, that is, $\alpha\, c_{MgGd}$ was a cut-off value. The initial molar density $c_{MgGd} = 6.73610^{-5}$ mol/mm^3 was calculated from the molar mass of magnesium and the measured volume and mass of the IB sample, and α was chosen as 0.4. The diffusivity D in Eq. (6) is set to 10^{-8} mm^2/s (Marvi-Mashhadi et al., 2021). At this point one needs to be aware not to over-interpret its physical effect. The rate of magnesium ion motion also depends on the (nodal) fluxes applied in the simulations. Hence the value of D is somehow arbitrary. The required iteration of the fluxes to meet the measured mass loss might give the interpretation that the combination of both, diffusivity and fluxes, lead to the observed state of corrosion.

The total amount of substance of a body, $n(t)$, is calculated as the sum of individual concentrations and volumes,

$$n(t) = \sum_i c_i(t)\, V_i\, H\left(c_i(t) - \alpha c_{MgGd}\right), \tag{10}$$

with H being the Heaviside function. The amount of substance at time $t = 0$ is used as a reference and is denoted as n_{start}. The mass loss, $\frac{\Delta m}{m_0}(t)$, is therefore calculated from:

$$\frac{\Delta m}{m_0}(t) = \frac{n_{start} - n(t)}{n_{start}}\,. \tag{11}$$

By iteratively simulating the mass diffusion process with different scale factors β, a given mass loss can be achieved that depends on the Weibull distribution. This procedure was implemented using a Python code together with the Finite Element Suite ABAQUS/Standard (Mangels, 2022).

4.3. Simulation of strength loss and failure

This section describes a procedure to predict the strength loss of arbitrary three-dimensional solids due to mass loss. It aims at replacing the scanning process described in chapter Section 3.2 by exploiting the diffusion model. As such, the spatial discretisation of the corroded sample becomes obsolete, and a mechanical simulation can be conducted on the basis of the initial geometry by using a damage model. The constitutive model described in Section 4.1 will be applied here.

A key point is the translation of the progress of corrosion as captured by the diffusion simulations to the mechanical model, which is explained in the following. As introduced in Section 4.2, the concentration (of the metallic phase) is described by a variable $c \in [0, c_{MgGd}]$. This concentration can then be related to the volume fraction of oxide which is assumed to be given by:

$$f_{Ox} = \begin{cases} 1 - \frac{c - \alpha c_{MgGd}}{(1-\alpha) c_{MgGd}} & \text{for} \quad c \geq \alpha c_{MgGd} \\ 1 & \text{for} \quad c < \alpha c_{MgGd} \end{cases}. \tag{12}$$

This renders $f_{Ox} = 0$ for $c = c_{MgGd}$, and $f_{Ox} = 1$ for $c \leq \alpha c_{MgGd}$. Assuming a simple rule of mixtures, the flow stress of the corroded material becomes

$$\sigma_F = \sigma_F(p, f_{Ox}) = \sigma_F(p)(1 - f_{Ox})\,, \tag{13}$$

where the "pure" oxide material ($f_{Ox} = 1$) is assumed to have no load-carrying capacity. In this equation, $\sigma_F(p)$ is still given by Eq. (4). A similar rule of mixtures was assumed for Young's modulus, that is, $E(f_{Ox}) = E_0(1 - f_{Ox})$.

f_{Ox} is assumed to take effect after a given period of corrosion but *prior* to the simulated mechanical test. That is, f_{Ox} pictures the mechanical effect of the corrosion product. By manipulating the result of the diffusion analysis by Eq. (12), the weakening of the material due to corrosion can be mapped to the relevant material points of the mechanical model. In the present case, concentrations given at nodal positions were interpolated to integration point values by a mapping tool available in the FE code Z-set (Besson et al., 1998) and subsequently read in as initial conditions.

4.4. Finite element models

For the simulation of the mass loss due to diffusion and for the mechanical analysis, identical spatial discretisations were used for each sample. The IB geometry was homogeneously meshed using 128,000 8-node diffusion elements (DC3D8 in ABAQUS) for the corrosion analysis and 8-node stress–strain elements with selective integration for the compression analysis with Z-set. For the mechanical analysis, displacements were prescribed on the quadratic faces of the IB parallel to the (x,y)-plane, A and A', see Fig. 4. Reaction forces were recorded from these nodes. The strain was calculated from these displacements normalised by the initial length of 8 mm.

For the tension analyses, typical plane dog-bone samples were considered in the simulations. In the following, they are referred to as micro flat tensile samples (MFT). Note that their geometry was different from the one of the TS samples used in the experiments. The reason for this difference was that we sought to avoid numerically triggered localisation effects expected for exactly prismatic geometries. Shoulder regions ensure that load transfer is sufficiently uniform in the gauge section. Additional geometrical imperfections were not used. Diffusion and tensile analyses used discretisations with 71,660 8-node diffusion elements (DC3D8 in ABAQUS) and 8-node stress–strain elements with selective integration for the tension analysis. Since the shoulders of the MFT samples solely serve as load transmitters, their effect in the diffusion analysis is irrelevant. Therefore, nodal fluxes were only applied on the four faces of the prismatic section, see Fig. 4. Axial displacements were applied for the simulation of the tensile tests on the shoulder surfaces A and A', see Fig. 4. The reaction forces divided by the initial cross section constituted the stress signal. The strain was calculated from the displacement difference in the parallel section. The failure strain was defined as the strain at maximum global stress of each sample. Since the material does not show severe necking in tension, this definition leads to similar results than considering the elongation at fracture.

5. Results

5.1. Assessment of experimental results on Mg-10Gd degradation

The morphologies and types of used specimens result in a different degradation behaviour. One representative immersion brick sample has been selected and is shown in Fig. 5. This sample is representative of most corroded immersion bricks as it has small pits all over its surface leading to a nearly homogeneous degradation after five weeks. For assessing the degradation behaviour of the tensile sticks qualitatively, the geometry as well as the ratio of surface to volume has to be considered. Opposite to the compact geometry of the immersion bricks, the tensile sticks are elongated with a larger surface area exposed to the immersion medium. Pitting corrosion and breaks of specimens were observed frequently, which prevented a comprehensive investigation.

The degradation of the immersion bricks was quantified via mass loss and release of Mg during degradation over five weeks. Fig. 6(a) shows the relative mass loss of immersion bricks increasing from a median of 0.8% after one week to a maximum of 3.5% over the corrosion time of five weeks. This was observed for both as prepared (ap, grey) and predeformed immersion bricks (def, red). Note that most recorded data points are close to each other in their respective group, which results in small standard deviations where these were not boosted by outliers, compare Fig. 6(a). Very similar median values were observed for the as-prepared and predeformed immersion bricks.

In addition to the mass loss, the Mg release and the corrosion rate, which is based on the mass loss, are shown in Fig. 6(b). Fig. 6(b) illustrates the fast degradation during the first week followed by an almost constant release up to the fifth week. The variance of values increased within the progress of the immersion test. Altogether, the qualitative evaluation of the degradation behaviour of the immersion bricks is confirmed by the quantitative analysis and can be described as relatively homogeneous with 3 outliers out of 50 specimens.

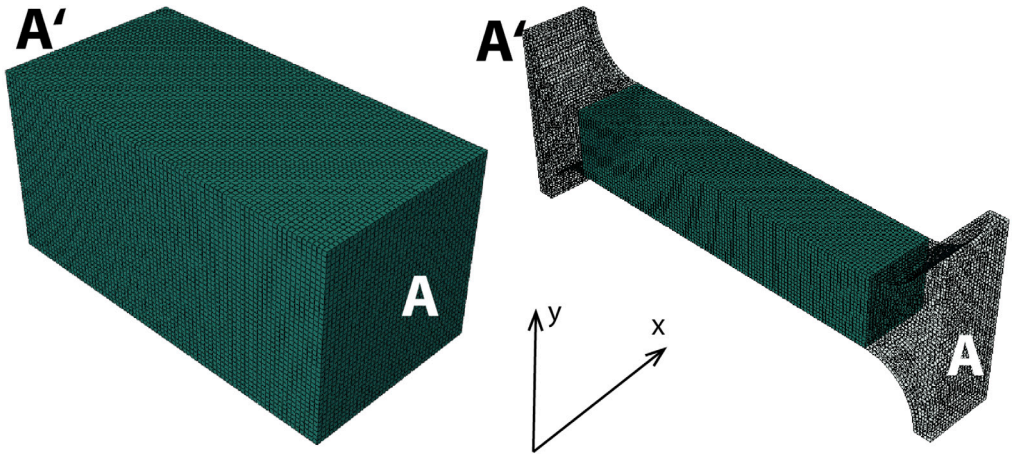

Fig. 4. Finite-element models of IB (left) and MFT (right). Nodal fluxes are prescribed on the outer surfaces appearing in green.

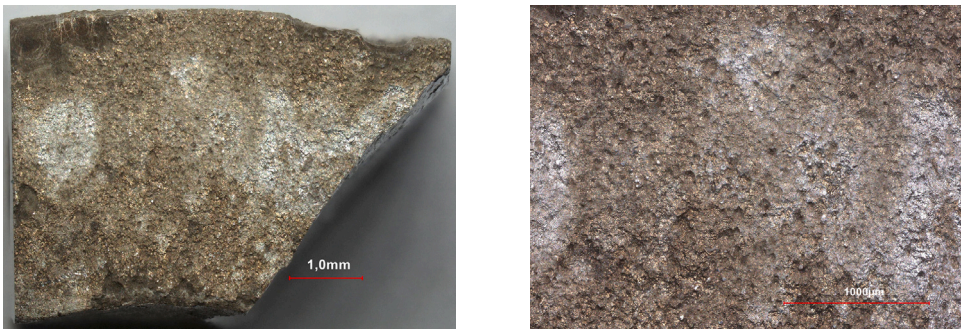

(a) Overview showing the slanted failure mode after compression

(b) detail of (a)

Fig. 5. Surface of a compression-loaded immersion bricks after five weeks of corrosion.

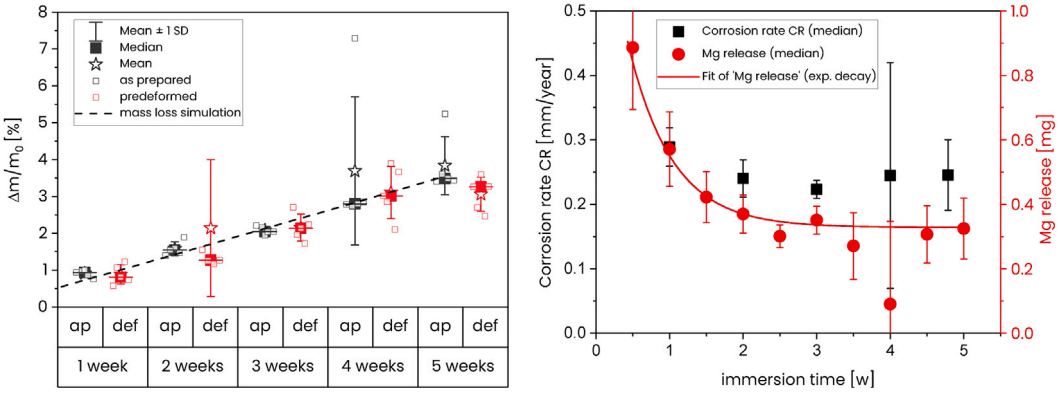

(a) Relative mass loss of as prepared (ap, black) and predeformed (def, red) Immersion Bricks

(b) Corrosion rate and magnesium release of as prepared samples

Fig. 6. Experimental results of the IB immersion tests (1 to 5 weeks).

5.2. Parameter calibration for the as-received material

FE simulations were conducted for IB and MFT samples to describe the observed measured force–displacement behaviour of the as-received material. From the tensile test, at first the parameters of the hardening law, Eq. (4), were calibrated. Second, the parameter k describing the strength differential effect in Eq. (3) was determined on the basis of the compression test. Finally, the parameters of the damage model were set to meet the failure point observed in the tensile tests. Table 2 shows the parameters producing the simulation results depicted in Fig. 7. Since the heads of the MFT samples were included in the FE model, strain localisation occurs diagonally in the central region of the samples. This is caused by slightly elevated strain in the middle and subsequent damage at that position. For more details on the localisation behaviour, readers are referred to Besson et al. (2003), which analyses discretisation effects and model symmetries.

5.3. Tensile behaviour of corroded TS-samples

From the set of corroded TS samples, six individual samples were selected, which showed significant corrosion signs near or in the middle of the test section. The specimens were immersed for one week (two

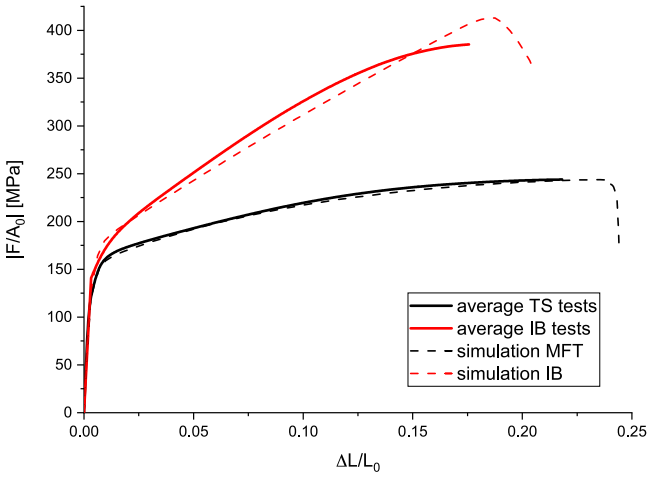

Fig. 7. Finite-element simulations of compression- and tension tests compared to the averaged TS and IB experiments.

Table 2
Calibrated model parameters of the plasticity and damage model.

Plasticity						
R_0 [MPa]	Q_1 [MPa]	Q_2 [MPa]	b_1	b_2	κ	k
111.5	226.8	46.5	5.1	472.0	2.0	−0.148
Damage						
ε_n	s_n	d_n				
0.24	0.015	1.0				

pieces), two weeks (one piece), three weeks (two pieces), and four weeks (one piece), see Table 3. Prior to mechanical testing, they were scanned following the procedure described in Section 3.2 to obtain the exact shape of the samples and of the corrosion product. The magnesium material domain in the simulations was defined based on the image segmentation (yellow mask in Fig. 1). Finite element simulations of the tensile tests were performed using the parameter of the as-received material, see Table 2. For the discretisation, tetrahedral volume elements (C3D4 in ABAQUS) were used. The results of the simulations are depicted in Fig. 8(a). The stress level of each individual sample could be met well. This indicates that the geometry of the corrosion pits was mapped sufficiently accurately to the finite element model for capturing the local reduction of cross section. It also confirms that the latter is primarily relevant for the strength loss caused by corrosion (van Gaalen et al., 2021). The failure strain defined as the strain at maximum global stress, however, was consistently overestimated in the simulations, see dashed lines in Fig. 8(a). This is, to a certain extent, expected since local porosities and micro-cracks caused by corrosion were not resolved in the CT scan. Hence, the damage nucleation strain had to be changed in order to capture these effects. ε_n was therefore reduced compared to the value given in Table 2 and set to 0.165, with the other parameters unchanged. This resulted in predictions represented by the solid lines noted "FEMmod" in Fig. 8(a). A summary focusing on the measured and predicted failure strains and their respective scatter is given in Fig. 8(b).

From the simulations described in this section, it can be concluded that in samples that have undergone already some corrosion, the mechanical characteristics of the not yet corroded material are largely the same as those of the as-received material. Only the effects related to surface roughness and micro-cracks reduce the load bearing capacity. The (global) failure strain can be predicted with reasonable accuracy once micro-cracks on the surface are considered as damage initiators. The degradation layer does not need to be taken into account in this context.

5.4. Prediction of the compression behaviour (IB)

Simulations of IB compression tests were performed using the same discretisation as shown in Fig. 4a. Motivated by the appearance of the corroded surfaces (see Fig. 5), the parameter a of the Weibull distribution, Eq. (8) was set to $a = 1.0$, rendering a moderately smooth distribution of nodal fluxes in the mass diffusion analysis. The surface appearance is similar in this case to the experiment, compare Figs. 9 and 5(b). The nodal fluxes were iterated to give the measured mass loss of 3.5% after five weeks, depicted in Fig. 6(a). The calculated concentration fields were mapped to the oxide volume fraction f_{Ox} following the procedure outlined in Section 4.3 for the points in time of one, two, three, four, and five weeks. For each of these stages, one simulation of the compression test was performed, rendering the results given in Fig. 10. While in the simulations a clear trend of stress reduction with immersion time prevails, this trend was less clear in the experiments. In Fig. 10(a), a single averaged stress–strain curve is presented for each corrosion stage to improve readability, whereas all experimental results are included in Fig. 8(b) for tensile specimens. Two power-law functions were fitted to visualise the decrease of maximum stress and failure strain (*i.e.* strain at maximum stress). The simulations meet the fitting functions very well. This indicates that the concept of sequential mass diffusion analysis and concentration–damage mapping is able to predict strength loss and reduction of failure strain in the time range considered.

It is worth mentioning that the change of the initial slope of the stress–strain curves of the corroded samples is caused by the roughness of the contacting surfaces, and is not related to a reduction of the net cross section of the samples. This effect could be captured in the simulations by adding two thin layers of elastic material to the surfaces exposed to compression load. Further, in these compression simulations, the damage nucleation strain, ε_n, was taken from the as-received material, $\varepsilon_n = 0.24$, because in compression surface micro-cracks caused by corrosion do not play a role (crack closure effect). Micro-cracks are relevant for the ductility in tension, but not in compression.

5.5. Prediction of the tensile behaviour (MFT) as a function of corrosion time

As already mentioned in Section 5.1, the corrosion of TS samples was less homogeneous than in the case of IB samples. Local attacks and pronounced pitting led to the breakage of many samples. After four weeks, only one sample could be taken for tensile testing, and after five weeks none of the initial five samples was left, see Table 3. This is represented in Fig. 11, where stress and strain maxima experienced during tensile testing of the corroded samples are shown.

To capture these results for the TS/MFT samples numerically, a high level of localisation for the mass diffusion analysis had to be chosen. $a = 0.01$ was selected here to seed fluxes on the sample surface. Further, the mass loss data experimentally acquired from the IB samples had to be adopted to the MFT samples. The relative volume losses were given as a function of the mean degradation depth t

$$\text{IB}: \quad V_{loss}^{rel} = 4\left(\frac{t}{w}\right)^3 - 8\left(\frac{t}{w}\right)^2 + 5\left(\frac{t}{w}\right) \tag{14}$$

$$\text{MFT}: \quad V_{loss}^{rel} = 4\left(\frac{t}{w}\right)^2 + 4\left(\frac{t}{w}\right), \tag{15}$$

with w being the characteristic length dimension of IB ($w = 4$ mm) and MFT ($w = 2$ mm). Provided that the mass density is the same for both samples, relative mass loss and relative volume loss are interchangeable. Solving (14) with $V_{loss}^{rel} = 0.035$ for t yields a degradation depth after five weeks of 0.028 mm for this sample. On the assumption that the corrosion rates are identical for IB and MFT samples, inserting this into (15) renders an equivalent volume loss of 5.74%, which was iterated in the mass diffusion analyses once the MFT sample is considered. Note that here only the four outer surfaces were mapped with nodal fluxes, since the corrosive medium can only attack from

Table 3
The tensile sticks' test and simulation history (TS: tensile stick).

ID	Corrosion time [w]	Tested	Simulated	ID	Corrosion time [w]	Tested	Simulated
TS-03	1	✓	*x*	TS-22	3	✓	*x*
TS-04	1	✓	*x*	TS-33	3	✓	x
TS-25	1	✓	✓	TS-34	3	x	x
TS-26	1	✓	x	TS-50	3	✓	✓
TS-46	1	✓	✓	TS-54	3	✓	✓
TS-07	2	✓	✓	TS-15	4	✓	✓
TS-08	2	x	x	TS-16	4	x	x
TS-29	2	✓	x	TS-38	4	x	x
TS-30	2	✓	x	TS-39	4	x	x
TS-48	2	x	x	TS-52	4	x	x
TS-11	3	x	x	TS-42	5	x	x
TS-12	3	x	x	TS-43	5	x	x
TS-21	3	✓	*x*				

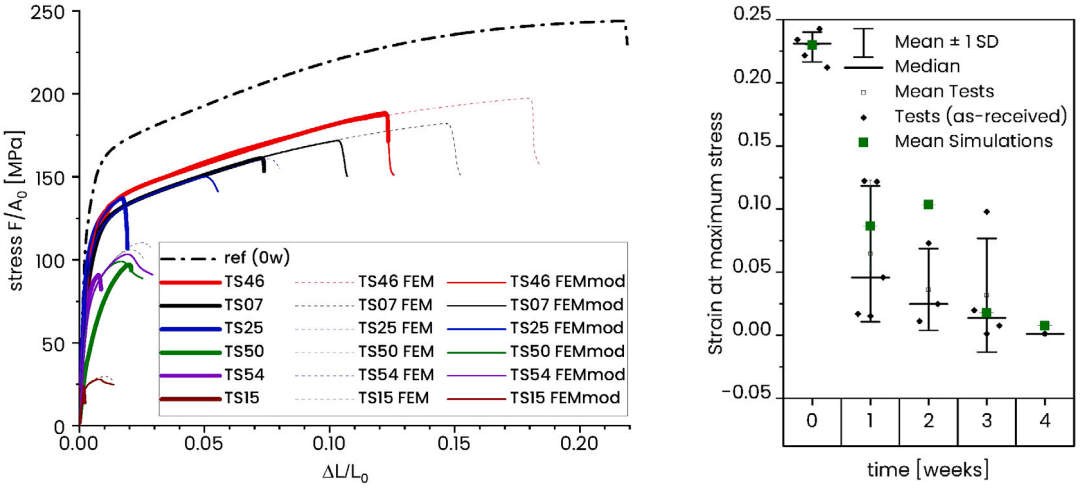

(a) Stress–strain behaviour of TS samples (sample designation see table 3)

(b) Failure strain statistics

Fig. 8. Simulation results of individual TS samples in comparison to tensile tests.

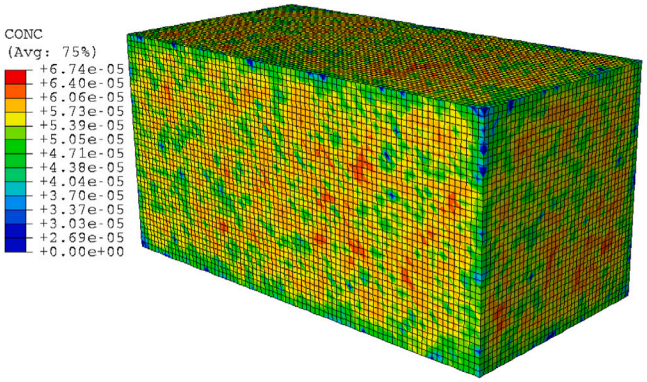

Fig. 9. Mass loss analysis of IB (a = 1.0): Magnesium concentration after five weeks.

these sides. The results of one representative mechanical analysis per point in time are illustrated in Fig. 11. The reduction in maximum stress was reasonably well captured by the simulations, with deficits, however, for longer corrosion times. The reduction of ductility was captured well for all corrosion times, see Fig. 11(b).

6. Discussion

There are different techniques and methods to determine the corrosion rate of metals. Considering the benefits of Mg-based biomaterials for medical applications, the description of the degradation behaviour under physiological conditions is particularly relevant (Esmaily et al., 2017). However, the selection of physiological test conditions and media increases the complexity of the system. The immersion in a cell culture medium provides small negatively and positively charged ions, small organic compounds as well as large peptides and proteins. All these components relate to different effects on the Mg corrosion behaviour. A high Cl^- content accelerates the corrosion, CO^{3-} bind free Mg^{2+} ions and form less soluble complexes (Agha et al., 2016). Most importantly, the interaction of material surface with proteins, which are introduced by the fetal serum, resulted in the complexation of Ca^{2+} and the formation of a more or less stable protection layer which may reduce the degradation rate (Helmholz et al., 2021a; Hou et al., 2019). Due to such complex interactions, the sensitivity of the test system to variations of the degradation conditions is higher compared to single salt solutions and ambient conditions. Standards were defined for testing the immersion behaviour of metallic medical devices in electrolytes as ISO 10993-15 standard (Anon, 2019), ASTM NACE/ASTM G31-12a standard, and ISO10933 part 12 for non flat, irregular samples. In the present study, the conditions were selected accordingly and slightly adapted. Immersion conditions were kept constant and equalled an electrolyte volume to test specimen surface area ratio of 0.125 mL/mm^2 for the IB samples, and to 0.020 mL/mm^2 for the TS samples. This represents a compromise between covering the whole sample body with a sufficient amount of immersion medium and meeting the recommendations of the mentioned guidelines. Nevertheless, differences in the corrosion behaviour between the IB and TS samples were observed. The more pronounced local degradation of the TS compared to the IB might be attributed to the different volume to surface ratio. In semi-static

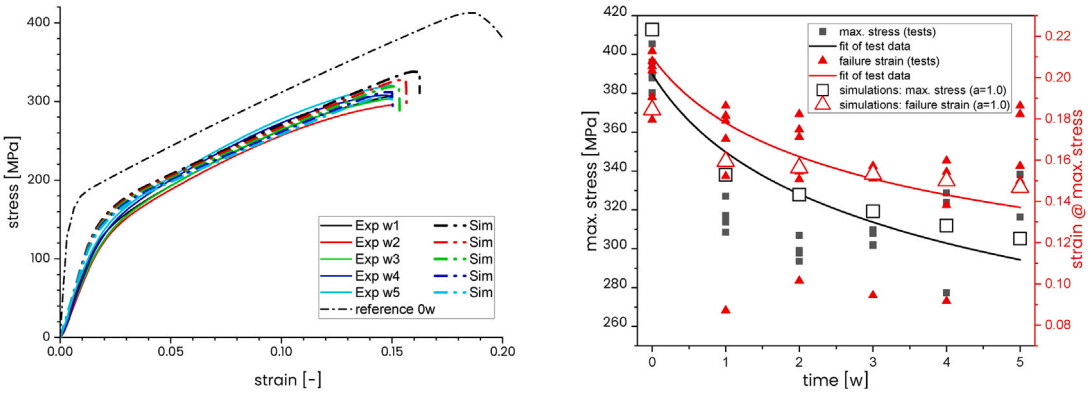

(a) Stress–strain behaviour of IB-samples

(b) Maximum stress and failure strain as a function of immersion time

Fig. 10. Results of IB compression tests in comparison to simulation results.

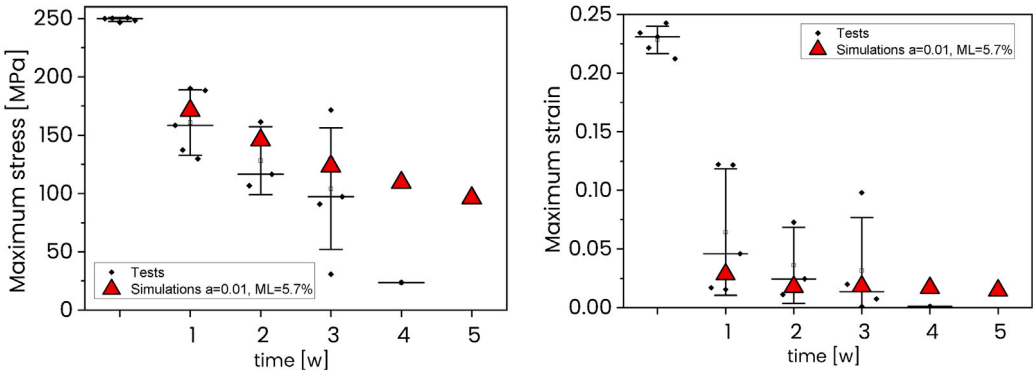

(a) Stress maxima

(b) Failure strains

Fig. 11. Experimental (TS) and numerical (MFT) results for $\Delta m/m_0 = 5.7\%$ and $a = 0.01$.

degradation tests, less volume per surface (ratio between test solution volume and test specimen surface area) leads to a faster increase in pH, which promotes dense deposit layer formation and subsequently should lower the degradation rate (Zhao et al., 2008). As pit initiation statistics very much vary with the alloying element distribution, grain boundary effects as well as surface defects, it is still possible to observe high degradation rates despite electrolyte and deposit effects. Within this study it was observed that corrosion was suppressed in 3.5% NaCl solutions at pH values higher than 12. Localised corrosion did not appear as already shown by Zeng et al. (2006). However, the cited work showed an influence of pH values on the distribution and morphology of corrosion pits. High pH values lead to more local corrosion with pit formation, limited by pH=12, above which corrosion was suppressed. This effect seems to be also existent in the present work, where the rapid increase in pH in the case of TS samples lead to severe local corrosion.

Due to the described differences in corrosion localisation, it was not expected that an identical Weibull distribution of fluxes, as considered in the case of IB samples, would produce the same results as the mechanical analyses of the TS/MFT samples. Apparently, such reuse of Weibull parameters is generally not possible even if the degrading systems are comparable. Due to the high sensitivity of the pit initiation mechanisms to small variations within the surface defect morphology as well as to the local electrolyte conditions, the application of IB/TS calibrated values to the MFT samples is, in general, not possible. If the degradation, in particular, becomes more heterogeneous, this aspect has to be kept in mind. As a consequence and as described in Section 5.5, $a = 0.01$ was chosen to adequately simulate the localised corrosion scenario of the tensile samples. To quantify the effect of the Weibull statistics, a numerical study was performed. An MFT sample was seeded for mass diffusion (weight loss) analyses with four different Weibull distributions, namely with $a = 1.0$, $a = 0.5$, $a = 0.1$, and $a = 0.01$. For each case, 10 realisations were generated, leading to 40 simulations in total. The fluxes were iteratively determined such that they resulted in the same global mass loss in all cases. Only the parallel sections of the sample were considered to be affected by corrosion. One realisation for each of the above four Weibull distributions is depicted in Fig. 12. Although the position of the nodal fluxes was randomly chosen in the parallel section, the simulations are comparable in the sense that the corrosion conditions were identical. The results of the subsequent mechanical analyses are depicted in Fig. 13. With increasing localisation, $a = 1.0 \rightarrow 0.01$, the maximum stress decreases by 52%. At the same time, the variation increases. Even more pronounced is the reduction of ductility, expressed by the average strain at maximum stress. Even for the "smooth" Weibull distribution of $a = 1.0$, an average reduction of ductility compared to the one of the as-received material of 49% is calculated. $a = 0.01$ renders a reduction of 91%. In essence, a high localisation level of corrosion leads to a moderate stress reduction, but to a drastic loss of ductility. In its principle, this is neither a contradiction nor surprising: Due to the low strain-hardening of the material, small changes in stress lead to large variations in strain. This is common for as-received material, but it also applies to corroded samples with non-uniform cross-sections.

The effect of the damage variable d in the analyses of failure is illustrated in Fig. 14. The mapped field of corrosion product f_{Ox} (see Fig. 14(a)) has two main effects on mechanics. First, it reduces the transfer of stresses via Eq. (13). Second, due to the in-homogeneity of the field, it triggers strain localisation in the remaining metallic material. The latter acts on the damage evolution, Eq. (5), and finally causes

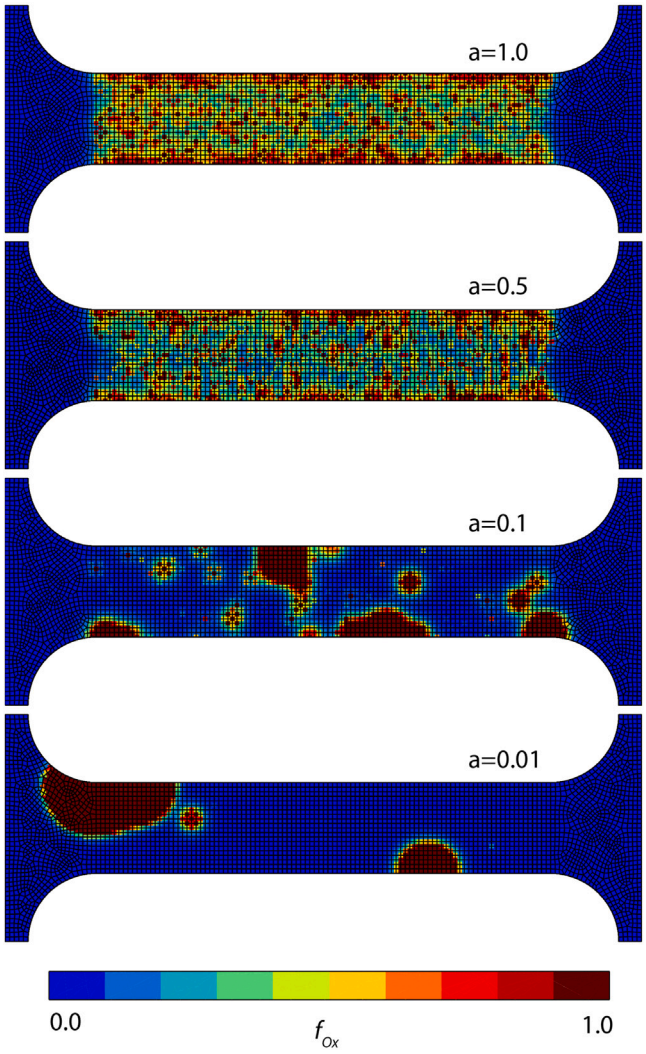

Fig. 12. Surface views of f_{Ox} for different configurations rendering the same mass loss (initial configurations prior to tensile testing).

cracks to develop from the surface, see Fig. 14(b). By this interaction, the effect of corrosion pitting can be accounted for in the mechanical model. Although the described model is of phenomenological nature, it appears to be versatile and hence useful for the assessment of medical implants undergoing corrosion, provided that the results of this in vitro study can be generalised towards in vivo problems. In the current mathematical formulation, it is capable of covering the whole range from perfectly uniform degradation to statistically distributed pitting corrosion and its superposition. Intergranular effects as well as effects related to hydrogen uptake are not explicitly modeled, but they are intrinsically included by the domain damage approach.

Commonly, FE analyses based on coupled damage models leading to material softening as utilised herein, show a mesh dependency. Therefore, in the computational study a dependency of results on the discretisation is expected. With increasing mesh refinement for a given element formulation, the localisation zone becomes smaller. Hence, the dissipated energy decreases with decreasing element size. While this effect has significant impact in the case of fracture toughness simulations, the influence in the case of tensile samples is less pronounced (Besson et al., 2001). Further, for the diffusion analysis it is expected that a higher density of nodes affects the degree of localisation of corrosion. To quantify both effects for the current model, simulations of mass diffusion and tension are conducted for a mesh with 563,400 elements (instead of the 71,660 elements for the simulations described above) for one realisation of the Weibull distribution with $a = 0.5$. The result of the mechanical analysis is included in Fig. 13(a) by green open symbols. The stress–strain behaviour is identical to the one obtained with the coarser mesh. The predicted ductility falls in the strain interval given by the other simulations. It can therefore be concluded that the conditions of equal mass loss lead to comparable results in case the discretisation is changed.

The damage model, Eqs. (2) and (5), is kept as simple as possible here. The assumed damage nucleation function solely depends on the plastic strain. The damage growth rate does not depend on the stress triaxiality. Consequently, the model does not consider the growth and coalescence of voids and defects. The well-known triaxiality-dependence of failure in ductile metals (Hancock and Mackenzie, 1976) cannot be described. This simplification, however, appears acceptable, since failure initiation of corroded samples happens at the surface where the triaxiality equals $1/3$. It is further in line with observations made for other magnesium wrought alloys, for which strain-based failure models revealed quantitatively good results (Steglich and Besson, 2021; Jeong and Steglich, 2020). The parameter calibration presented here is robust, since it is possible to predict failure both in tension and compression. Note that the latter is triggered by a plastic instability, which depends on the length-to-width ratio of the compressed sample (IB: 2:1).

The application of the model to other Mg alloys is possible. It has to be considered that the intensity of pit formation depends on the alloying elements (see e.g. Kannan and Raman, 2008), and its distribution. For example, calcium addition enhances the pitting corrosion resistance of magnesium alloys significantly, and the surface properties as well (Boland et al., 2018). In parallel, a comparison of grinded and not grinded samples of the same alloy revealed a delay of corrosion by a factor of 50 times for grinded samples. This sensitivity of pit formation is very challenging, but not impossible to model on the macroscale. As each Mg processing and treatment has a certain impact on secondary phases (distribution and impurities), it can be assumed that each material requires its own Weibull parameter calibration to predict its pitting corrosion and mechanical behaviour.

7. Conclusions

In this paper, a computational framework was developed to study the effect of corrosion on the mechanical behaviour of Mg samples. Corrosion is modeled by a mass-diffusion type model accounting for, in general, parallel occurrence of uniform and localised corrosion. To model the statistical effects governing localised corrosion attacks, Weibull statistics is used. In our corrosion model, the overall loss of mass of a sample has to be prescribed (e.g., based on experimental data) to normalise the spatially distributed mass fluxes in the corrosion model properly. The mechanical behaviour of Mg is modeled by a state-of-the-art CPB plasticity model with a coupled damage model. This allows us to study how Mg degradation in immersed samples reduces the mechanical strength over time. We performed a large number of corrosion experiments and mechanical tests to validate our computational framework in a laboratory setting. It turned out that our framework could predict for both tension and compression tests the experimentally observed loss of mechanical strength due to corrosion when using extremely sharp Weibull distributions representing pitting corrosion. In addition to the strength loss due to corrosion, the reduced ductility could be numerically predicted.

Our study confirmed the importance to consider the surface/volume effect of the samples during corrosion testing and numerical analysis. It was shown that the conversion of the volume mass loss data via the surface related mean corrosion depth can be an appropriate way to do so. With consideration of calibrated Weibull statistics (e.g. $a = 1$ approximates uniform-like corrosion, $a < 0.1$ approximates strong pitting events) the macroscopic mechanical behaviour of the implant material can be adequately computed. Adaption of the approach to

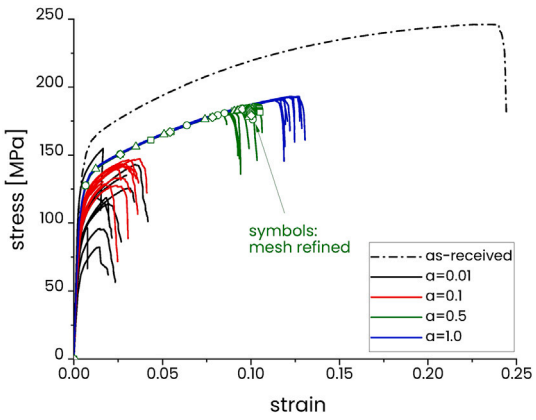

(a) Simulated macroscopic stress–strain curves

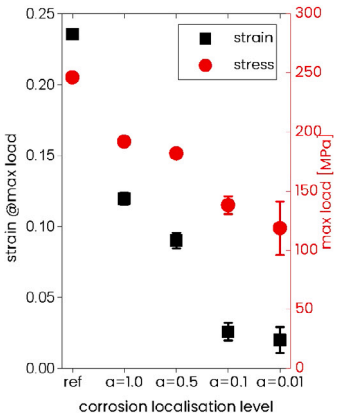

(b) Mean values and standard deviations of maximum stress and failure strain

Fig. 13. Numerical study to quantify the effect of Weibull statistics on the tensile behaviour of MFT samples: $a = 1.0$, $a = 0.5$, $a = 0.1$, and $a = 0.01$.

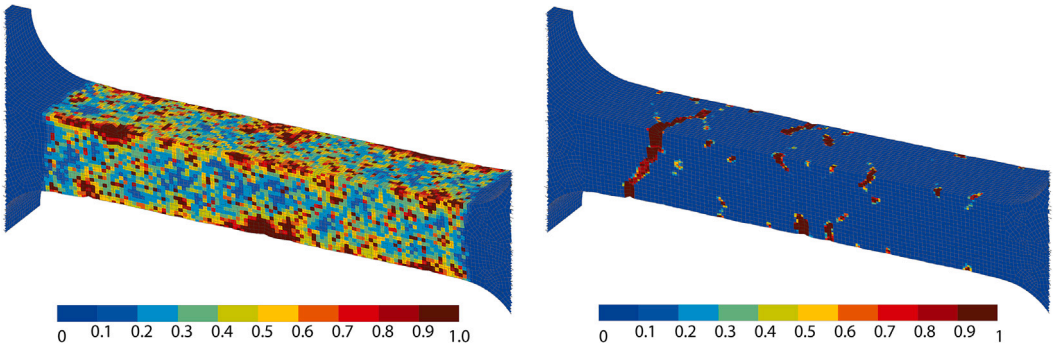

(a) Fraction of corrosion product f_{Ox}

(b) Damage variable d

Fig. 14. Mechanical analysis of MFT under tension (a = 0.5).

other Mg alloys and materials suffering pitting corrosion is possible but requires careful Weibull parameter calibration. A general limitation of our current computational framework is the need to prescribe the overall mass loss to calibrate the boundary conditions of the corrosion model. To overcome this limitation, in the future more sophisticated corrosion models are required that can predict the rate of mass loss if the geometry and material of the sample as well as the chemical properties of its environment are given. Such a more advanced corrosion model could, for example, rely on a phase-field approach or a peridynamics approach (Hermann et al., 2022; Shojaei et al., 2020).

CRediT authorship contribution statement

Dirk Steglich: Writing – review & editing, Writing – original draft, Validation, Supervision, Project administration, Methodology, Investigation, Data curation, Conceptualization. **Jacques Besson:** Writing – original draft, Supervision, Methodology, Conceptualization. **Inken Reinke:** Writing – original draft, Investigation, Formal analysis, Data curation. **Heike Helmholz:** Writing – original draft, Project administration, Methodology, Investigation, Data curation. **Monika Luczak:** Investigation, Formal analysis. **Vasil M. Garamus:** Writing – original draft, Investigation. **Björn Wiese:** Writing – original draft, Methodology, Investigation. **Daniel Höche:** Writing – original draft, Supervision. **Christian J. Cyron:** Writing – review & editing, Funding acquisition. **Regine Willumeit-Römer:** Writing – review & editing, Funding acquisition.

Declaration of competing interest

The authors declare that they have no known competing financial interests or personal relationships that could have appeared to influence the work reported in this paper.

Data availability

Data will be made available on request.

Acknowledgements

The authors like to thank Danny Mangels for his diligent scripting and model calibration, Jürgen Markmann and Kay Erdmann for their assistance during mechanical testing, Mohammad Mavi Mashadi for providing example input files out of his previous work, and Rainer Falkenberg for fruitful discussions. The advices of Annette Havelberg on proofreading are very much appreciated.

References

Agha, N.A., Feyerabend, F., Mihailova, B., Heidrich, S., Bismayer, U., Willumeit-Römer, R., 2016. Magnesium degradation influenced by buffering salts in concentrations typical of in vitro and in vivo models. Mater. Sci. Eng. C 58, 817–825. http://dx.doi.org/10.1016/j.msec.2015.09.067.

Anon, 2019. ISO 10993 Biological evaluation of medical devices — Part 15: Identification and quantification of degradation products from metals and alloys. ISO 10993.

Besson, J., Leriche, R., Foerch, R., Cailletaud, G., 1998. Object-oriented programming applied to the finite element method Part II. Application to material behaviors. Revue Eur. Elem. 7 (5), 567–588. http://dx.doi.org/10.1080/12506559.1998.10511322.

Besson, J., Steglich, D., Brocks, W., 2001. Modeling of crack growth in round bars and plane strain specimens. Int. J. Solids Struct. 38, 8259–8284.

Besson, J., Steglich, D., Brocks, W., 2003. Modeling of plane strain ductile rupture. Int. J. Plast. 19, 1517–1541.

Boland, E.L., Shirazi, R.N., Grogan, J.A., McHugh, P.E., 2018. Mechanical and corrosion testing of magnesium WE43 specimens for pitting corrosion model calibration. Adv. Eng. Mater. 20 (10), http://dx.doi.org/10.1002/adem.201800656.

Cazacu, O., Plunkett, B., Barlat, F., 2006. Orthotropic yield criterion for hexagonal closed packed metals. Int. J. Plast. 22, 1171–1194.

Chu, C., Needleman, A., 1980. Void nucleation effects in biaxially stretched sheets. J. Eng. Mater. Technol.-Trans. ASME 102, 249–256.

Dahms, M., Höche, D., Ahmad Agha, N., Feyerabend, F., Willumeit-Römer, R., 2018. A simple model for long-time degradation of magnesium under physiological conditions. Mater. Corros. 69 (2), 191–196. http://dx.doi.org/10.1002/maco.201709461.

Esmaily, M., Svensson, J., Fajardo, S., Birbilis, N., Frankel, G., Virtanen, S., Arrabal, R., Thomas, S., Johansson, L., 2017. Fundamentals and advances in magnesium alloy corrosion. Prog. Mater. Sci. 89, 92–193. http://dx.doi.org/10.1016/j.pmatsci.2017.04.011.

Feyerabend, F., Fischer, J., Holtz, J., Witte, F., Willumeit, R., Drücker, H., Vogt, C., Hort, N., 2010. Evaluation of short-term effects of rare earth and other elements used in magnesium alloys on primary cells and cell lines. Acta Biomater. 6 (5), 1834–1842. http://dx.doi.org/10.1016/j.actbio.2009.09.024.

Gastaldi, D., Sassi, V., Petrini, L., Vedani, M., Trasatti, S., Migliavacca, F., 2011. Continuum damage model for bioresorbable magnesium alloy devices — Application to coronary stents. J. Mech. Behav. Biomed. Mater. 4 (3), 352–365. http://dx.doi.org/10.1016/j.jmbbm.2010.11.003.

Gawlik, M.M., Wiese, B., Desharnais, V., Ebel, T., Willumeit-Römer, R., 2018. The effect of surface treatments on the degradation of biomedical Mg alloys-a review paper. Materials 11 (12), http://dx.doi.org/10.3390/ma11122561, Cited by: 24; All Open Access, Gold Open Access, Green Open Access.

Gawlik, M.M., Wiese, B., Welle, A., González, J., Desharnais, V., Harmuth, J., Ebel, T., Willumeit-Römer, R., 2019. Acetic acid etching of Mg-xGd alloys. Metals 9 (2), http://dx.doi.org/10.3390/met9020117, Cited by: 4; All Open Access, Gold Open Access, Green Open Access.

Gazenbiller, E., Arya, V., Reitz, R., Engler, T., Oechsner, M., Höche, D., 2021. Statistical analysis of AA-1050 localized corrosion in anhydrous ethanol. Corros. Sci. 179, 109137.

Globig, P., Willumeit-Römer, R., Martini, F., Mazzoni, E., Luthringer-Feyerabend, B.J.C., 2020. Optimizing an osteosarcoma-fibroblast coculture model to study antitumoral activity of magnesium-based biomaterials. Int. J. Mol. Sci. 21 (14), 1–18. http://dx.doi.org/10.3390/ijms21145099, Cited by: 7; All Open Access, Gold Open Access, Green Open Access.

Grogan, J.A., Leen, S.B., McHugh, P.E., 2014. A physical corrosion model for bioabsorbable metal stents. Acta Biomater. 10 (5), 2313–2322. http://dx.doi.org/10.1016/j.actbio.2013.12.059.

Grogan, J.A., O'Brien, B.J., Leen, S.B., McHugh, P.E., 2011. A corrosion model for bioabsorbable metallic stents. Acta Biomater. 7 (9), 3523–3533. http://dx.doi.org/10.1016/j.actbio.2011.05.032.

Hancock, J., Mackenzie, A., 1976. On the mechanisms of ductile failure in high-strength steels subjected to multi-axial stress-states. J. Mech. Phys. Solids 24, 147–169.

Harmuth, J., Wiese, B., Bohlen, J., Ebel, T., Willumeit-Römer, R., 2019. Wide range mechanical customization of Mg-Gd alloys with low degradation rates by extrusion. Front. Mater. 6, http://dx.doi.org/10.3389/fmats.2019.00201.

Helmholz, H., Adejube, B., Luthringer-feyerabend, B., Willumeit-römer, R., 2021a. In vitro investigation on degradable mg-based biomaterial under the impact of the serum glycoprotein fetuin. Materials 14 (17), http://dx.doi.org/10.3390/ma14175005.

Helmholz, H., Will, O., Penate-Medina, T., Humbert, J., Damm, T., Luthringer-Feyerabend, B., Willumeit-Römer, R., Glüer, C.-C., Penate-Medina, O., 2021b. Tissue responses after implantation of biodegradable Mg alloys evaluated by multimodality 3D micro-bioimaging in vivo. J. Biomed. Mater. Res. A 109 (8), 1521–1529. http://dx.doi.org/10.1002/jbm.a.37148.

Hermann, A., Shojaei, A., Steglich, D., Höche, D., Zeller-Plumhoff, B., Cyron, C., 2022. Combining peridynamic and finite element simulations to capture the corrosion of degradable bone implants and to predict their residual strength. Int. J. Mech. Sci. 220, 107143. http://dx.doi.org/10.1016/j.ijmecsci.2022.107143.

Hort, N., Huang, Y., Fechner, D., Störmer, M., Blawert, C., Witte, F., Vogt, C., Drücker, H., Willumeit, R., Kainer, K., Feyerabend, F., 2010. Magnesium alloys as implant materials-Principles of property design for Mg-RE alloys. Acta Biomater. 6 (5), 1714–1725. http://dx.doi.org/10.1016/j.actbio.2009.09.010.

Hou, R.-Q., Scharnagl, N., Willumeit-Römer, R., Feyerabend, F., 2019. Different effects of single protein vs. protein mixtures on magnesium degradation under cell culture conditions. Acta Biomater. 98, 256–268. http://dx.doi.org/10.1016/j.actbio.2019.02.013, 10th BIOMETAL2018 - International Symposium on Biodegradable Metals.

Jafarzadeh, S., Chen, Z., Bobaru, F., 2019. Computational modeling of pitting corrosion. Corros. Rev. 37 (5), 419–439. http://dx.doi.org/10.1515/corrrev-2019-0049.

Jeong, Y., Steglich, D., 2020. Modelling-assisted description of anisotropic edge failure in magnesium sheet alloy under mixed-mode loading. Int. J. Mech. Sci. 181, 105680. http://dx.doi.org/10.1016/j.ijmecsci.2020.105680.

Kannan, M.B., Raman, R.K.S., 2008. In vitro degradation and mechanical integrity of calcium-containing magnesium alloys in modified-simulated body fluid. Biomaterials 29 (15), 2306–2314. http://dx.doi.org/10.1016/j.biomaterials.2008.02.003.

Krüger, D., Galli, S., Zeller-Plumhoff, B., Wieland, D.F., Peruzzi, N., Wiese, B., Heuser, P., Moosmann, J., Wennerberg, A., Willumeit-Römer, R., 2022. High-resolution ex vivo analysis of the degradation and osseointegration of Mg-xGd implant screws in 3D. Bioact. Mater. 13, 37–52. http://dx.doi.org/10.1016/j.bioactmat.2021.10.041.

Krüger, D., Zeller-Plumhoff, B., Wiese, B., Yi, S., Zuber, M., Wieland, D.F., Moosmann, J., Willumeit-Römer, R., 2021. Assessing the microstructure and in vitro degradation behavior of Mg-xGd screw implants using μ CT. J. Magnes. Alloys 9 (6), 2207–2222. http://dx.doi.org/10.1016/j.jma.2021.07.029.

Lin, X.S., Wu, X., Wu, K., Chen, J., Tan, L., Witte, F., Yang, H., Mantovani, D., Zhou, H., Liang, C., Yang, Q., Yang, K., Yang, L., 2022. Biodegradable Mg-based alloys: biological implications and restorative opportunities. Int. Mater. Rev. 1–39. http://dx.doi.org/10.1080/09506608.2022.2079367.

Mangels, D., 2022. Simulating the Influence of Corrosion on the Mechanical Properties of a Magnesium Alloy for Bone Implants (Ph.D. thesis). TUHH, ICM.

Marvi-Mashhadi, M., Ali, W., Li, M., González, C., Llorca, J., 2021. Simulation of corrosion and mechanical degradation of additively manufactured Mg scaffolds in simulated body fluid. J. Mech. Behav. Biomed. Mater. 104881. http://dx.doi.org/10.1016/j.jmbbm.2021.104881.

Myrissa, A., Martinelli, E., Szakács, G., Berger, L., Eichler, J., Fischerauer, S.F., Kleinhans, C., Hort, N., Schäfer, U., Weinberg, A.M., 2016. In vivo degradation of binary magnesium alloys – a long-term study. BioNanoMaterials 17 (3–4), 121–130. http://dx.doi.org/10.1515/bnm-2016-0006.

NACE, 2016. Standard Guide for Laboratory Immersion Corrosion Testing of Metals. NACE lntemationa / ASTM lntemalional, pp. 92–101.

Nidadavolu, E.P.S., Feyerabend, F., Ebel, T., Willumeit-Römer, R., Dahms, M., 2016. On the determination of magnesium degradation rates under physiological conditions. Materials 9 (8), 627, URL https://www.mdpi.com/1996-1944/9/8/627.

Otsu, N., 1979. Threshold Selection Method from gray-level Histograms. IEEE Trans. Syst. Man Cybern. 9 (1), 62–66. http://dx.doi.org/10.1109/TSMC.1979.4310076.

Shojaei, A., Hermann, A., Seleson, P., Cyron, C., 2020. Dirichlet absorbing boundary conditions for classical and peridynamic diffusion-type models. Comput. Mech. 773–793.

Steglich, D., Besson, J., 2021. Prediction of deformation and failure anisotropy for thin magnesium sheets under mixed-mode loading. Mech. Mater. 163, 104064. http://dx.doi.org/10.1016/j.mechmat.2021.104064.

van Gaalen, K., Gremse, F., Benn, F., McHugh, P.E., Kopp, A., Vaughan, T.J., 2021. Automated ex-situ detection of pitting corrosion and its effect on the mechanical integrity of rare earth magnesium alloy - WE43. Bioact. Mater. http://dx.doi.org/10.1016/j.bioactmat.2021.06.024.

Xu, Y.-L., Wang, L., Huang, M., Gensch, F., Kainer, K.U., Hort, N., 2018. The effect of solid solute and precipitate phase on Young's modulus of binary Mg–RE alloys. Adv. Eng. Mater. 20 (10), http://dx.doi.org/10.1002/adem.201800271, Cited by: 11.

Zeng, R.-C., Zhang, J., Huang, W.-J., Dietzel, W., Kainer, K., Blanert, C., Ke, W., 2006. Review of studies on corrosion of magnesium alloys. Trans. Nonferr. Met. Soc. China 16, s763–s771. http://dx.doi.org/10.1016/S1003-6326(06)60297-5.

Zhang, Y., 2020. Influence of Intermetallic Amount on the Degradability of mg-RE (Nd/gd) Alloys Under Physiological Conditions (Ph.D. thesis). RWTH Aachen University.

Zhao, M.-C., Liu, M., Song, G.-L., Atrens, A., 2008. Influence of pH and chloride ion concentration on the corrosion of Mg alloy ZE41. Corros. Sci. 50 (11), 3168–3178. http://dx.doi.org/10.1016/j.corsci.2008.08.023.